arXiv:astro-ph/9701083v1 15 Jan 1997

INSTABILITIES AND MIXING IN SN 1993J

Kohichi IWAMOTO, Timothy R. YOUNG, Naohito NAKASATO,
Toshikazu SHIGEYAMA, Ken'ichi NOMOTO
Department of Astronomy, School of Science, University of Tokyo,
Bunkyo-ku, Tokyo 113, Japan

Izumi HACHISU
Department of Earth Science and Astronomy, College of Arts and Sciences, University of Tokyo,
Meguro-ku, Tokyo 153, Japan

and

Hideyuki SAIO
Department of Astronomy, Faculty of Science, Tohoku University Sendai, Japan

ABSTRACT

Rayleigh-Taylor (R-T) instabilities in the explosion of SN 1993J are investigated by means of two-dimensional hydrodynamical simulations. It is found that the extent of mixing is sensitive to the progenitor's core mass and the envelope mass. Because the helium core mass (3 - 4 $M_\odot$) is smaller than that of SN 1987A, R-T instabilities at the He/C+O interfaces develop to induce a large scale mixing in the helium core, while the instability is relatively weak at the H/He interface due to the small envelope mass. The predicted abundance distribution, in particular the amount of the ^{56}Ni mixing, is compared with those required in the theoretical light curves and the late time optical spectra. This enables us to specify the progenitor of SN 1993J in some detail.

Subject headings: hydrodynamics: the R-T instability — instability: mixing — stars: supernovae — supernovae: individual (SN 1993J)

1. INTRODUCTION

SN 1993J has been identified as a Type IIb supernova (SN IIb) from the spectral changes which show growing features of helium and oxygen, and from the optical light curve which shows double peaks (Wheeler & Filippenko 1996; Baron et al. 1995 for reviews and references therein). These features are distinct from those of previously known Type II supernovae (SNe II). It was obvious that the peculiar light curve of SN 1993J cannot be accounted for by an explosion of an ordinary red supergiant with a massive hydrogen-rich envelope, which produces a light curve of a SN II-P; instead, it can be well reproduced as the explosion of a red-supergiant whose hydrogen-rich envelope is as small as $< 1\ M_\odot$ (Nomoto et al. 1993; Podsiadlowski et al. 1993; Shigeyama et al. 1994; Bartunov et al. 1994; Utrobin 1994; Woosley et al. 1994; Young et al. 1995). The progenitor of SN 1993J is likely to have lost most of its H-rich envelope due to the interaction with its companion star in a binary system.

Constraints on mixing in the ejecta of SN 1993J come from both observed spectra and photometry. Spectroscopically, the asymmetric profiles of the [O I] and [Mg I] emission lines at late times indicate mixing in the ejecta (Spyromilio 1994; Wang & Hu 1994). Shigeyama et al. (1994) first examined two extreme cases of mixing in their light curve modeling (i.e., with complete homogeneous mixing inside the helium layers and without mixing) and favored mixing of ^{56}Ni in SN 1993J. Woosley et al. (1994) also favored mixing of ^{56}Ni in their light curve modeling.

The occurrence of mixing and clumpiness in the supernova ejecta was first confirmed in SN 1987A. One clear confirmation is the early detection of hard X-rays and γ-rays originated from the decays of ^{56}Ni and ^{56}Co (e.g., Kumagai et al. 1989). Stimulated by these observations and theory, a number of multidimensional simulations have been performed to show that the R-T instability develops indeed in the ejecta of SN 1987A (Arnett et al. 1989; Hachisu et al. 1990, 1992; Müller et al. 1991; Den et al. 1990). It was found that the instability is weak at the He/C+O and Ni/O interfaces but strong at the H/He interface, which can be expected from the large helium core mass $\sim 6\ M_\odot$ and the massive hydrogen-rich envelope $\sim 10\ M_\odot$. In SN 1987A, the large scale mixing of nickel was induced by falling spikes of hydrogen which penetrated into deep inner layers.

Later, it has been recognized that the occurrence of mixing and clumping in the supernova ejecta can occur also in other types of supernovae and that the effect on their light curves can provide interesting diagnostics of the internal structure of the progenitors. The extent of mixing and clumpiness affect the light curve and spectra. A number of hydrodynamical simulations have shown that the R-T instabilities arise in the Type II-P explosions of red-supergiants (Herant & Woosley 1994; Shigeyama et al. 1996) and helium star models of Type Ib supernovae (Hachisu et al. 1991, 1994) as in SN 1987A.

These studies indicate the importance of multidimensional simulations of instabilities in supernova ejecta. This is particularly interesting for SN 1993J because its presupernova structure is suggested to be quite different from other supernovae. Conversely, we may strongly constrain the progenitor's mass and structure because the R-T instabilities are sensitive to the density structure of the progenitor. Despite such importance, no such simulation has been conducted before. Therefore, we have carried out two dimensional hydrodynamical simulations for the R-T instability in the ejecta of SN 1993J to examine the extent of mixing and the resultant abundance distributions quantitatively. In parallel, we have calculated bolometric light curves for several explosion models with various extent of mixing and compared them with the observations. These results would enable us to constrain the progenitor model, which would be useful to understand the still debated presupernova evolution.

In the next section, the presupernova models for SN 1993J are described. Results of the linear stability analysis and the 2D hydrodynamical simulations are shown in §3 and §4, respectively. The effects of ^{56}Ni mixing on the optical light curve are discussed in §5. Finally we summarize some constraints on the explosion models.

2. HYDRODYNAMICAL MODELS

2.1. Presupernova Models of the Progenitor

The progenitor models are constructed following Shigeyama et al. (1994). We use the presupernova helium cores of masses $M_\alpha = 3.3 M_\odot$ and $4 M_\odot$ (Nomoto & Hashimoto 1988), which are evolved from the main-sequence stars of $M_{ms} = 13M_\odot$ and $15M_\odot$, respectively. The adopted main-sequence masses are consistent with the inferred progenitor's luminosity (Hashimoto, Iwamoto, & Nomoto 1993). We assume that the star retained only a small mass H-rich envelope after a large amount of mass loss due to the merging with a small mass companion star (Nomoto et al. 1995, 1996). The hydrostatic and thermal equilibrium H/He envelope models are constructed for various masses $M_{\rm env}$, radii $R_{\rm i}$, and the helium abundance Y to smoothly fit to the helium core. The model parameters are summarized in Table 1. The density distributions for 3H11, 3H41, 4H13, and 4H47 are shown in Figure 1.

These models have large helium abundances in the envelope. Such an enhancement of helium is expected from the gradient of helium abundance in the deepest layers of the envelope (see, e.g., Saio, Nomoto, & Kato 1988). If most of the hydrogen-rich envelope is removed, the helium-rich layer is exposed as seen in Yamaoka et al. (1991) and Nomoto et al. (1991); they have calculated mass loss from the initially 13 $M_\odot$ star, which reduces the envelope mass down to 0.3 $M_\odot$ and enhances the average helium mass fraction up to ~ 0.5 at the termination of Roche lobe overflow (see also Woosley et al. 1994).

2.2. Hydrodynamics of Explosion

We simulate the core collapse-induced explosion by depositing thermal energy at the mass cut (a partition between neutron star and ejecta) generating a strong outward shock wave. The deposited energy is set to produce the kinetic energy of explosion $E = 1 \times 10^{51}$ erg. The mass cut is chosen to produce 0.1 $M_\odot$ of ^{56}Ni. The propagation of the shock wave and hydrodynamics of the ejecta are calculated with a one dimensional Lagrangian PPM code (Shigeyama et al. 1991). Nucleosynthesis yields behind the shock wave are nearly the same as obtained in the 3.3 $M_\odot$ and 4.0 $M_\odot$ He core models (Shigeyama et al. 1990; Iwamoto et al. 1994; Thielemann, Nomoto, & Hashimoto 1996).

Figure 2 shows the evolution of the density and pressure profiles in the ejecta of 4H13 and 3H11, respectively. When the shock wave passes through the He/C+O interface, the ejecta around the shock front undergoes a strong deceleration, which forms an inwardly propagating reverse shock. This stage corresponds to the profiles at $t = 10$ sec in Figure 2. Between the two shock waves, there appears a region with pressure inversion. Then the R-T instability is expected to arise around the interface due to the opposite signs of the density and pressure gradients. When the shock wave arrives at the H/He interface, it is strongly decelerated again in the same manner as it passed the He/C+O interface. This is shown in the profiles at $t = 1000$ sec in Figure 2.

This complicated behavior of hydrodynamics, the alternate acceleration and deceleration, can be explained by behavior of the self-similar solutions of the blast shock in spherically expanding gas with a power law density distribution $\rho \propto r^{-n}$ (Sedov 1959; Chevalier 1976). In these solutions, the forward shock wave is accelerated for $n > 3$, while the shock is decelerated for $n < 3$ (Müller et al. 1989; Herant & Woosley 1994). Figure 3 shows $\rho\, r^3$ against the enclosed mass M_r for the initial density profiles of 4H13 and 3H11, respectively. It is seen that there are two distinct regions where the shock wave should be decelerated and the R-T instability would grow.

3. LINEAR STABILITY ANALYSIS

In this section, we present an estimate of the R-T growth by the linear stability analysis. Our method is basically the same as that used for SN 1987A by Ebisuzaki et al.(1990), Benz & Thielemann (1991), and Müller et al. (1991). In the classical case that two homogeneous fluids are stratified in the gravitational field, a linear growth rate is given as (Chandrasekhar 1981)

$$G_{RT}^2 = \frac{\rho_+ - \rho_-}{\rho_+ + \rho_-} k g, \tag{1}$$

where ρ_+ and ρ_- are the densities in the upper and lower layers, respectively, and k is the wavenumber of the perturbation, g the acceleration due to the gravity. This formula can be applied to the shocked ejecta of a supernova by replacing g with the effective gravity $g_{\rm eff}$ defined as

$$g_{\rm eff} = -g - \frac{1}{\rho}\frac{dP}{dr} \simeq -\frac{1}{\rho}\frac{dP}{dr}. \tag{2}$$

The pressure gradient term dominates in the strongly decelerated blast wave and the stellar gravity is negligibly small in the expanding ejecta. Equations (1) and (2) show that the ejecta gets

R-T unstable if the density and pressure gradients have opposite signs,

$$\frac{dP}{dr}\frac{d\rho}{dr} < 0. \tag{3}$$

We calculate the growth factor of the amplitude at each layer, ζ/ζ_0, by integrating the growth rate at each stage of spherically symmetric explosion models as

$$\frac{\zeta}{\zeta_0} = \exp\left[\int_0^t Re(G_{RT}(t^{'}))dt^{'}\right], \tag{4}$$

where ζ_0 is the initial amplitude of the perturbation and $Re(G_{RT})$ indicates the real part of the growth rate. As a linear growth rate, we take that of the fastest growing mode with the wavelength of about pressure scale height. The formula of the growth rate for the continuous density distribution (Chandrasekhar 1981) reduces to the following expression based on the above assumption:

$$G_{RT}^2 \simeq -\frac{1}{\gamma}\frac{c_s^2}{1+\pi^2}\frac{1}{H_\rho H_P}. \tag{5}$$

Here γ is the adiabatic index, c_s the adiabatic sound velocity, and H_ρ and H_P are the density and pressure scale heights, respectively, which are defined as

$$H_\rho = \frac{d\ r}{d\ \ln\rho}, \qquad H_P = \frac{d\ r}{d\ \ln P}. \tag{6}$$

Note that the linear stability analysis is not valid after the instability develops into the nonlinear phase. However, it is still meaningful to see qualitatively which regions of the ejecta are unstable. We calculate the R-T growth by equation (4) in parallel with one dimensional hydrodynamical simulations. Figure 4a shows the amplitude ζ/ζ_0 versus enclosed mass for both 3H41 and 4H47 at $t = 1$ day after the explosion.

There appear three distinct unstable regions: (1) the He/C+O interface around $M_r = 1.8$ $M_\odot$ (3H41) and 2.1 $M_\odot$ (4H47), (2) the H/He interface around $M_r = 3.3$ $M_\odot$ (3H41) and 4.0 $M_\odot$ (4H47), and (3) the surface region near the density inversion as seen in Figure 1. These regions are coincident with those expected from the behavior of ρr^3 in Figure 3. For 3H11 and 4H13, models with a smaller mass envelope, the growth is almost the same as for 3H41 and 4H13, respectively, but slightly different due to the different envelope structure (Fig.4b).

Figures 4a and 4b also show that at the He/C+O interface the growth is somewhat larger for 3H models than for 4H models. This is because the mass ratio between the He layer and the C-Ni core is larger in the 3.3 $M_\odot$ He core than in the 4 $M_\odot$ core so that the C-Ni core undergoes larger deceleration (Hachisu et al. 1991).

4. 2-D SIMULATIONS

We carry out two dimensional hydrodynamical simulations to follow a nonlinear growth of the R-T instabilities and mixing. The linear stability analysis indicates that the instability would grow in some particular regions, i.e, at the He/C+O interface, the H/He interface, and near the surface. The radius at the He/C+O interface is about $\sim 1\ R_\odot$ for both progenitor models, being two orders of magnitudes smaller than that of the H/He interface. When the shock wave reaches the H/He interface, the instability at the He/C+O interface has already ceased to grow. For these reasons, we examine the instabilities in the He core and near the core/envelope boundary in separate calculations to avoid a significant numerical diffusion due to unnecessary rezoning.

Our code is a standard third order TVD (Total-Variation-Diminishing) scheme with a preprocessing flux-limiter using the Roe's approximate Riemann solver (Hachisu et al. 1992, 1994). It has second order accuracy in time by using two-step time integration. We make several improvements in treating the advection of the chemical composition of the fluid. The advection equations of the mass fractions are solved as parts of the extended Roe matrix, which enables us to treat them consistently with the Euler equations constraining the sum of the mass fractions to be unity. This new method is advantageous for accurately obtaining the extent of mixing.

We use an equation of state with a constant adiabatic index 4/3, which is a good approximation here since the ejecta remains in the radiation dominant phase because of high temperatures. We use cylindrical coordinates with 513 grid points in each axis, R and Z. Several rezonings are still necessary even if the mixing in the inner and outer part is studied separately. When the shock wave reaches just inside the numerical boundary, we double the mesh size and remap all the flow variables onto the new grid system. Each physical quantity $q(2i-1, 2j-1)$ in the old grid is projected to $q(i, j)$ in a quarter of the new computational area. The initial profiles are inserted in the remaining part.

At the beginning of calculation, we apply random perturbations to the velocity field interior of the shock front (Hachisu et al. 1994). The latitudinal angle is divided into n pieces and the velocity field is perturbed in each area of π/n angles as

$$v_r = v_0(1 + \epsilon(2\mathrm{rmd}([n\theta/\pi]) - 1)), \qquad v_\theta = 0, \tag{7}$$

where rmd(i; integer) is a sequence of uniform random numbers in the range from 0 to 1 and $[x]$ denotes the maximum integer that cannot exceed x. In the present study, the amplitude of the perturbation is assumed to be $\epsilon = 0.05$ in all cases. The extent of mixing is expected to be independent of mesh resolutions with this large amplitude of initial perturbation (Hachisu et al. 1992, 1994).

Figures 5a and 5b show the density contour near the He/C+O interface for 3H41 (at $t = 174$ sec) and 4H47 (at 5.34×10^4 sec), respectively. Each contour is drawn with a logarithmically equal interval. It is seen that mushroom-like fingers are developed in the He core. This clearly shows that the R-T instability has grown to its nonlinear stage and a large scale mixing of the elements occurred in the velocity space within the He core.

Figures 6a and 6b show the density contour in the outer part near the H/He interface for 3H41 (at $t = 4 \times 10^4$ sec) and 4H47 (at 5×10^5 sec), respectively. The R-T instability also grows due to the steep density gradient above the interface. However, the finger-like structures near the bottom of the H-rich envelope are not developed so much as in the inner core region so that the extent of mixing is relatively small. This is due to the small hydrogen-rich envelope mass and thus a weak deceleration.

Near the He/C+O interface in the core, the R-T growth tends to be larger for smaller He core mass as discussed for the linear stability analysis. Such a dependence of mixing on the structure of the progenitors has been shown by Hachisu et al. (1990, 1991, 1994) for their models of SN 1987A and Type Ib supernovae. For SN 1993J, we expect that the R-T instability at the H/He interface is much weaker than in SN 1987A because of the smaller envelope mass. On the other hand, the density gradient in the He core of SN1993J is steeper than that of SN 1987A because of the smaller core mass. Therefore, we predict that the He/C+O interface in SN 1993J is the most unstable region and a large scale mixing would be induced in the He core.

We calculate averaged radial distributions of the chemical compositions in the ejecta from the results of the two dimensional simulations. Figures 7 and 8 show the resultant abundance distributions against M_r for 3H41 and 4H47, respectively. It is seen that ^{56}Ni is mixed out to $M_r = 1.0\ M_\odot$ for 3H41 but only to $M_r = 0.5\ M_\odot$ for 4H47. Mixing of carbon and oxygen into the He layer is significant for both cases. Hydrogen is not largely mixed down to the He core for both cases due to the small envelope mass. If the mass of the hydrogen-rich envelope is smaller (as in 3H11 and 4H13 in Table 1.), the expanding core undergoes smaller deceleration so that the velocities of H, He, O, and Fe would be higher. Comparisons of the observed expansion velocities of H, He, O, and Fe with those predicted by the models will be made in §6.

5. OPTICAL LIGHT CURVE AND MIXING

As described in §1, the optical light curve of SN 1993J showed a unique behavior, with neither a clear plateau nor a monotonic decline. It rapidly declined after the first maximum, then rose to the second peak in 10-15 days, and finally followed by a gradually declining tail. The basic feature of this peculiar light curve can be accounted for with the Type IIb model, namely, the explosion of a red supergiant whose hydrogen-rich envelope is quite thin.

The light curve analysis of SN1993J has shown that the progenitor radius and mass are the main parameters that determine the shape of the light curve (e.g., Shigeyama et al. 1994; Woosley et al. 1994; Young et al. 1995). These studies have also noted some effects of ^{56}Ni mixing on the light curve shape. In the earlier sections, we have shown that ^{56}Ni is indeed mixed into the He layer but the degree of mixing depends on the progenitor's mass. Here we present more detailed study of the optical light curve in order to determine the amount of mixing of ^{56}Ni and examine whether the plausible model for SN 1993J can be identified. More details as well as the dependence on other parameters will be presented in Young et al. (1996).

We calculate bolometric light curves for 3H11, 3H41, and 4H47 with several changes in the ^{56}Ni distribution. The light curve code is the same as used in Young et al. (1995), which is the flux-limited radiative transfer code assuming LTE. Figures 9 - 11 compare the theoretical light curves of these models with the observed bolometric light curve (Richmond et al. 1994; Lewis et al. 1994) with a distance to M81 of 3.63 Mpc (Freedman et al. 1995). In each of the figures, three degrees of mixing are used; for example, "Mix 0.2 $M_\odot$" implies that ^{56}Ni is uniformly mixed from the center to $M_r = 0.2\ M_\odot$. The explosion energy and ^{56}Ni masses are held at $E = 1 \times 10^{51}$ ergs and 0.1 $M_\odot$, respectively, for all the models.

Generally, the first peak in the light curve is produced by the radiation field established in the shock heated H/He envelope, while the second peak is formed by diffusive leak of the deposited energy due to the radioactive decay of ^{56}Ni and ^{56}Co. Finally the light curve enters an exponential declining tail due to the ^{56}Co decay.

The most obvious feature that the mixing effects is the tail of the light curve. The declining rate of the tail is faster for more extensive mixing and for smaller mass He core, since the ejecta is more transparent to γ-rays. The no mixing case for 3H11 has a brighter tail and a shallower slope and is brighter than the observations. On the contrary, mixing to 1.0 - 1.5 $M_\odot$ for 3H41 gives a tail that is too steep to be compatible with observations.

The effects of mixing on the light curve shape around the dip at day 20 and the second peak are also seen. With more extensive mixing, the heating effect of radioactive decays starts to appear earlier so that the dip is shallower and the second peak is reached earlier. These effects are relatively small for 3H11 but much more important for 3H41 and 4H47 due to the thicker envelope. For 3H41 a critical mixing mass is found to be out to $M_r = 1\ M_\odot$, with which the fit at 20 days is improved. However mixing to this extent gives a tail that is too steep as seen in Figure 10. For 4H47, the tail is reproduced well with the mixing up to 1.8 - 2.2 $M_\odot$, and the mixing out to 2.2 $M_\odot$ gives a good fit to the dip at 20 days.

To summarize, the observed light curve shape around the dip, the second peak, and its tail are well reproduced with the model 4H47 if mixing extends to $M_r \sim 2\ M_\odot$. For 3H11 and 3H41, the mixing produces better fit to the tail (solid line) but tends to form a dip at day 20. Improvement of the radiative transfer code might improve the fit at the dip for 3H models.

6. DISCUSSION

We compare the calculated abundance distributions as a function of M_r (measured from the bottom of the ejecta) (Figures 7 and 8) and the expansion velocity (Figures 12 – 15) with the degree of mixing required from the light curve modeling and the spectroscopic observations of SN 1993J.

After the expansion becomes homologous ($v \propto r$), the expansion velocity of each layer remains constant so that it can be directly compared with the observed velocities of various elements. In the hydrodynamical models, the expansion velocity $v_{\rm exp}$ depends on the explosion energy $E_{\rm exp}$ and the total mass of the ejecta $M_{\rm ej}$ as

$$v_{\rm exp} \propto E_{\rm exp}^{1/2} M_{\rm ej}^{-1/2}. \tag{8}$$

We have tried another 2-D simulation for 3H41 with a different explosion energy of $E_{\rm exp} = 0.6 \times 10^{51}$ erg and found little difference in the degree of mixing in the M_r space compared with the case of $E_{\rm exp} = 1.0 \times 10^{51}$ erg. Therefore, we can safely assume that the velocity of each element in our models scales to the explosion energy as in equation (8).

Houck and Fransson (1996) have analyzed the spectra of SN 1993J and find that the observed spectra are well reproduced by their synthetic spectra if (1) some iron extends to at least 3000 km s^{-1} in the velocity space, (2) $\sim 0.5\ M_\odot$ oxygen occupies 1000 - 4000 km s^{-1}, and (3) the bulk of hydrogen lies between 8500 - 10,000 km s^{-1}. For the hydrogen velocity, however, the minimum velocity has been determined to be $v_{\rm Hmin} \sim 7500$ km s^{-1} from the inner edge of the Hα line profile at late times (Patat, Chugai & Mazzali 1995).

The coexistence of oxygen and iron at 1000 - 3000 km s^{-1} implies the mixing of O and Fe in the velocity space, if O and Fe are separated at first. Our calculations show that even the larger mass 3H model, 3H41, has the maximum velocity of oxygen as high as 6500 km s^{-1}. Thus, as for the oxygen velocity, 3H models are not preferable. The maximum velocity of oxygen in 4H47 is $\sim$ 4300 km s^{-1} , which is relatively agreeable.

The maximum velocity of ^{56}Ni (decaying eventually to Fe) is sensitive to the He core mass, i.e., $v_{\rm Ni} \sim 6000$ km s^{-1} for 3H models and 3000 km s^{-1} for 4H models. This is because the He core with a smaller mass expands faster and undergoes more extensive mixing as discussed in §3. Compared with the observations, $v_{\rm Ni}$ in 3H models is too fast. In 4H models, $v_{\rm Ni} \sim 3000$ km s^{-1} is marginally acceptable but a little too low.

The minimum velocity of hydrogen, $v_{\rm Hmin}$, depends mainly on the mass of the H/He envelope, since the effect of mixing at the core/envelope boundary is not significant. For 3H11 (3H41) and 4H13 (4H47), $v_{\rm Hmin} \sim 8500$ (7000) km s^{-1} and 9000 (6300) km s^{-1}, respectively. Thus, if we adopt $v_{\rm Hmin} \sim 7500$ km s^{-1} from the late time Hα profile, the envelope mass of $\sim$ 0.3 - 0.4 $M_\odot$ would be more consistent with the observed hydrogen velocities than $\sim$ 0.1 $M_\odot$.

We find in §4 that the calculated light curves give the best fit to the observations if ^{56}Ni is mixed up to $M_r \sim 2.2$ $M_\odot$ for 4H47 and to 0.5 - 1.5 $M_\odot$ for 3H41 and 3H11. However, in our simulations of the R-T instabilities, ^{56}Ni is mixed up to $M_r \sim 0.5$ $M_\odot$ for 4H models and to 1.0 $M_\odot$ for 3H models. Thus the calculated degree of ^{56}Ni mixing is too small in 4H models, while being consistent with the light curve modeling in 3H models. We should note, however, that the agreement between the calculated and observed light curves is better for 4H47 than for 3H41.

The determination of oxygen mass from the late time spectra would be another way to determine the progenitor's mass. Houck & Fransson (1996) estimated that the oxygen mass is $\sim$ 0.5 $M_\odot$. In the explosion models, the produced oxygen masses are 0.21, 0.42, and 1.5 $M_\odot$ for the He cores of 3.3, 4, and 6 $M_\odot$, respectively. (Thielemann et al. 1996). Thus the 4 $M_\odot$ core model gives the more consistent oxygen mass.

The inconsistencies of the mixing in the 3H and 4H models with the spectroscopic and photometric observations can be reconciled as follows.

(1) For 3H models, the fast decline of the tail may be improved if the explosion energy is as low as 0.8 × 10^{51} ergs. This is also suggested ¿from the X-ray light curve analysis (Suzuki &

Nomoto 1995).

(2) For 4H models, to be consistent with the observed light curve, the mixing of ^{56}Ni should be much more extensive than that occurs in the 2D simulation. Such a large scale mixing would require an extremely large initial perturbations, which might be due to the neutrino-induced R-T instabilities (Herant, Benz, & Colgate 1992; Burrows, Hayes, & Fryxell 1995; Janka & Müller 1996), the convective oxygen shell burning just before the collapse (Bazan & Arnett 1995), or the spiral-in of a companion star in the common envelope scenario (Nomoto et al. 1995, 1996).

The instabilities in the H-rich envelope might be more extensive than our models show. An additional perturbation, such as an asymmetric structure (Höflich 1995) due to the spiral-in of the companion star into the envelope (Nomoto et al. 1995, 1996) would cause more mixing. It is important to know whether the density distribution in the H-rich envelope is largely changed due to the possible development of the above instabilities, because the X-ray light curves (Zimmermann et al. 1994; Kohmura et al. 1994) has been found to be sensitive to the envelope structure of the ejecta (Suzuki & Nomoto 1995; Fransson, Lundqvist, & Chevalier 1996).

7. CONCLUSIONS

We have investigated the Rayleigh-Taylor instabilities in the ejecta of SN 1993J with a linear analysis of spherically symmetric explosion models and with a two-dimensional hydrodynamical simulations. We find the following conclusions.

1. The instability at the He/C+O interface develops to induce a large scale mixing because of the relatively small He core mass.

2. The instability at the H/He interface is weak because of the small hydrogen-rich envelope mass.

These features (1,2) are in contrast to SN 1987A which had the more massive He core and the envelope. The extent of mixing of heavy elements (Ni and C+O) is sensitive to the core mass. For the smaller core mass, the R-T instability is stronger and causes more extensive mixing due to the smaller mass ratio between the core and the He layer.

3. The optical light curves are calculated with a parameterized degree of mixing. The oberved light curve is well reproduced if substantial amount of ^{56}Ni mixing occurs.

4. The calculated abundance distributions of the ejecta against the expansion velocity are compared with the observed velocities of Ni, O, and H. The model with the 3.3 $M_\odot$ He core and the hydrogen-rich envelope of 0.3-0.4 $M_\odot$ can well reproduce the observational feature of SN 1993J, if the explosion energy is as low as $\sim 0.8 \times 10^{51}$ ergs. The model with the 4 $M_\odot$ He core and the ~ 0.5 $M_\odot$ envelope is also a good alternative, if ^{56}Ni is more extensively mixed than our present calculations, possibly due to much larger initial perturbations.

This work has been supported in part by the grant-in-Aid for Scientific Research (05242102, 06233101) and COE research (07CE2002) of the Ministry of Education, Science, and Culture in Japan, and the fellowship of the Japan Society for the Promotion of Science for Japanese Junior Scientists (4227). The computation was carried out on Fujitsu VPP-500 at the Institute of Physical and Chemical Research (RIKEN) and the Institute of Space an Astronautical Science (ISAS), and VPP-300 at the National Astronomical Observatory in Japan (NAO, Tokyo).

REFERENCES

Arnett W. D., Fryxell B. A., and Muller E., 1989, ApJ, 341, L63

Baron, E., Hauschildt, P. H., & Young, T. R., 1995, Phys. Rep., 256, 23

Bazan, G., & Arnett, P., 1994, ApJ, 433, L41

Benz, W., & Thielemann, F,-K., 1990, ApJ, 348, L17

Bartunov, O. S., Blinnikov, S. I., Pavlyuk, N. N., & Tsvetkov, D. Yu., 1994, A&A, 281, L53

Burrows, A., Hayes, J., & Fryxell, B.A., 1995, ApJ, 450, 830

Chevalier, R.A., 1976, ApJ, 207, 872

Chandrasekhar S.,1981, Hydrodynamic and Hydromagnetic Stability (New York:Dover)

Den M., Yoshida T. and Yamada Y., 1990, Progr. Theor. Phys., 83, 723

Filippenko A.V., et al. , 1992, AJ, 104, 1543

Fransson, C., Lundqvist, P., & Chevalier, R.A., 1996, ApJ, 461, 993

Freedman, W.L., et al., 1994, ApJ, 427, 628

Hachisu I., Matsuda T., Nomoto K., and Shigeyama T., 1990, ApJ, 358, L57

Hachisu I., Matsuda T., Nomoto K., and Shigeyama T., 1991, ApJ, 368, L27

Hachisu I., Matsuda T., Nomoto K., and Shigeyama T., 1992, ApJ, 390, 230

Hachisu I., Matsuda T., Nomoto K., and Shigeyama T., 1994, A&AS, 104, 341

Hashimoto M., Iwamoto K., Nomoto K., 1993, ApJ, 414, L105

Herant M., Benz W. & Colgate S., 1992, ApJ, 395, 642

Herant, M., & Woosley, S.E., 1994, ApJ, 425, 814

Höflich, P., 1995, ApJ, 440, 821

Houck, M., & Fransson, S., 1996, ApJ, 456, 811

Iwamoto, K., 1994, Master Thesis, University of Tokyo

Janka & Müller, 1996, A&A, in press

Kohmura, Y., et al., 1994, PASJ, 46, L157

Kumagai, S., Shigeyama, T., Nomoto, K., Itoh, M., Nishimura, J., & Tsuruta, S., 1989, ApJ, 345, 412

Lewis, J. R., et al. , 1994, MNRAS, 266, L27

Müller E., Hillebrandt, W., Orio, M., Höflich, P., Mönchmeyer, R., Fryxell, B.A., 1989, A&A, 220, 167

Müller E., Fryxell B.A., and Arnett W. D., 1991, A&A, 251, 505

Nomoto K., Hashimoto M., 1988, Phys. Rep., 163, 13

Nomoto K., Kumagai S., Shigeyama T., 1991, Gamma-Ray Line Astrophysics: AIP Conference Proceedings 232, eds. P. Durouchoux & N. Prantzos (New York: AIP), p.236

Nomoto, K., Suzuki, T., Shigeyama, T., Kumagai, S., Yamaoka, H., & Saio, H., 1993, Nature, 364, 507

Nomoto, K., Iwamoto, K., & Suzuki, T., 1995, Phys. Rep., 256, 173

Nomoto, K., Iwamoto, K., Suzuki, T., Pols, O.R., Yamaoka, H., Hashimoto, M., Höflich, P., Van den Heuvel, E.P.J., 1996, IAU Symposium 165, Compact stars in Binaries, eds. J. Paradij, E.P.J. van den Heuvel, & E. Kuulkers (Dordrecht: Kluwer), p. 119

Patat, F., Chugai, N., & Mazzali, P.A., 1995, A&A, 299, 715

Podsiadlowski, Ph., Hsu, J. J. L., Joss, P. C., & Ross, R. R., 1993, Nature, 364, 509

Richmond, M.W., Treffers, R.R., Filippenko, A.V., Piak, Y., Leibundgut, B., Schulman, E., & Cox, C.V., 1994, AJ, 107, 1022

Saio H., Nomoto K., and Kato M., 1988, Nature, 334, 508

Schmidt, B., Eastman, R., Kirshner, R., et al., 1993, Nature, 364, 600

Sedov, L.I., 1959, Similarity and Dimensional Methods in Mechanics (New York: Academic Press)

Shigeyama T., and Nomoto K., 1990, ApJ, 360, 242

Shigeyama, T., Suzuki, T., Kumagai, S., Nomoto, K., Saio, H., & Yamaoka, H., 1994, ApJ, 420, 341

Shigeyama, T., Iwamoto, K., Hachisu, I., Nomoto, K., 1996, IAU colloq. 145 Supernovae and Supernova Remnants, eds. R. McCray and Z. Wang (Cambridge: Cambdridge University Press), p.129

Spyromilio J., 1994, MNRAS, 266, 61

Suzuki, T., & Nomoto, K., 1995, ApJ, 455, 658

Thielemann, F.-K., Nomoto, K., & Hashimoto, M., 1996, ApJ, 460, 408

Utrobin, V., 1994, A&A, 281, L89

Wang, L., & Hu, J.Y., 1994, Nature, 369, 380

Wheeler, J. C., & Filippenko, A.V., 1995, in IAU colloq. 145 Supernovae and Supernova Remnants, eds. R. McCray and Z. Wang (Cambridge: Cambdridge University Press), p. 241

Woosley, S. E., Eastman, R. G., Weaver, T. A., & Pinto, P.A., 1994, ApJ, 429, 300

Yamaoka, H., & Nomoto, K., 1991, ESO/EIPC Workshop:SN1987A and other Supernovae, eds. I.J. Danziger & Kjär (Garching: ESO), p. 193

Young, T. R., Baron, E., & Branch D., 1995, ApJ, 449, L51

Young, T. R., Nomoto, K., Shigeyama, T., & Iwamoto, K., 1996, in preparation

Zimmerman H. U., et al., 1994, Nature, 367, 621

This preprint was prepared with the AAS LATEX macros v4.0.

Figure Captions

Fig. 1 – Density structures of the progenitor models at the onset of collapse.

Fig. 2 – Changes in the density and pressure profiles for (a) 4H13 and (b) 3H11. Each label indicates the time after the explosion; **1**: 0 sec, **2**: 10 sec, **3**: 100 sec, **4**: 1000 sec, **5**: 10,000 sec.

Fig. 3 – Plots of ρr^3 against enclosed mass $M_r/M_\odot$ for 4H13 (upper) and 3H11 (lower).

Fig. 4 – The Rayleigh-Taylor growth as a function of enclosed mass $M_r/M_\odot$ (a) for 3H41 (upper) and 4H47 (lower), and (b) for 3H11 (upper) and 4H13 (lower).

Fig. 5 – Density contours for (a) 3H41 (174 sec) and (b) 4H47 (149 sec).

Fig. 6 – Density contours for (a) 3H41 (5.34×10^4 sec) and (b) 4H47 (3.95×10^4 sec).

Fig. 7 – The averaged radial distribution of several elements as a function of M_r measured from the bottom of the ejecta for 3H41. Shown are the mass fractions of ^{56}Ni (solid), C+O (dotted), He (dashed), and H (long-dashed).

Fig. 8 – Same as Figure 7 but for 4H47.

Fig. 9 – Calculated bolometric light curves for 3H11 as compared with the observations of SN 1993J.

Fig. 10 – Same as Figure 9 but for 3H41.

Fig. 11 – Same as Figure 9 but for 4H47.

Fig. 12 – The averaged radial distribution of several elements as a function of the expansion velocity for 3H11. Shown are the mass fractions of ^{56}Ni (solid), C+O (dotted), He (dashed), and H (long-dashed).

Fig. 13 – Same as Figure 12 but for 3H41.

Fig. 14 – Same as Figure 12 but for 4H13.

Fig. 15 – Same as Figure 12 but for 4H47.

Table 1: Parameters for the progenitor models of SN 1993J

Name	$M_{\mathrm{env}}/M_{\odot}$	$M_{\mathrm{ej}}/M_{\odot}$	$M_{\mathrm{Ni}}/M_{\odot}$	$R_i/R_{\odot}$	$L/L_{\odot}$	Y	E_{exp}(10^{51} erg)
3H11	0.11	2.06	0.1	450	4.1×10^4	0.54	1.0
3H41	0.41	2.36	0.1	450	4.1×10^4	0.54	1.0
4H13	0.13	2.78	0.1	580	6.8×10^4	0.56	1.0
4H47	0.47	3.12	0.1	350	6.8×10^4	0.79	1.0

M_{env}: envelope mass, M_{ej}: total ejecta mass, M_{Ni}: ^{56}Ni mass. R_i: initial radii,

L: presupernova luminosity, Y: helium mass fraction in the envelope.

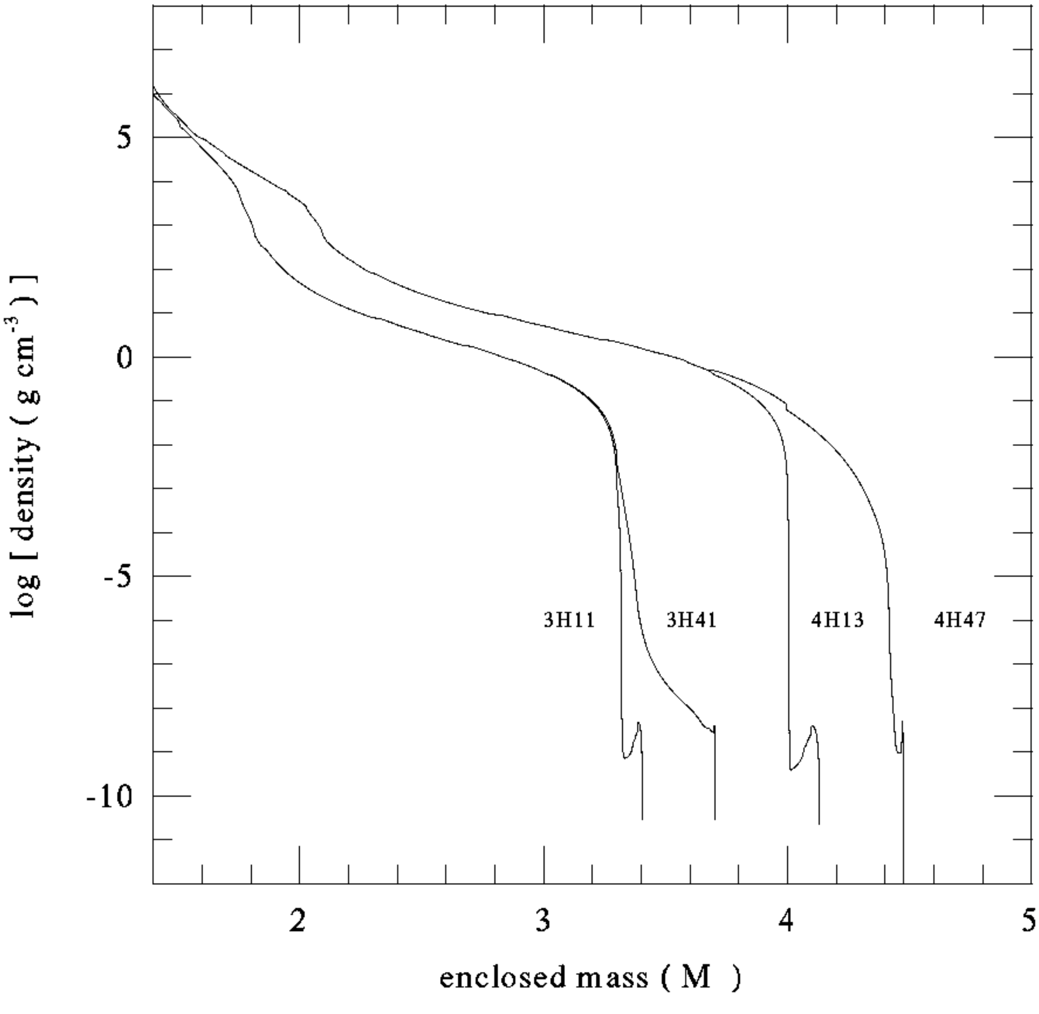

5
0
-5
-10
2
3
4
5
log [density (g cm^{-3})]
enclosed mass (M)
3H11
3H41
4H13
4H47

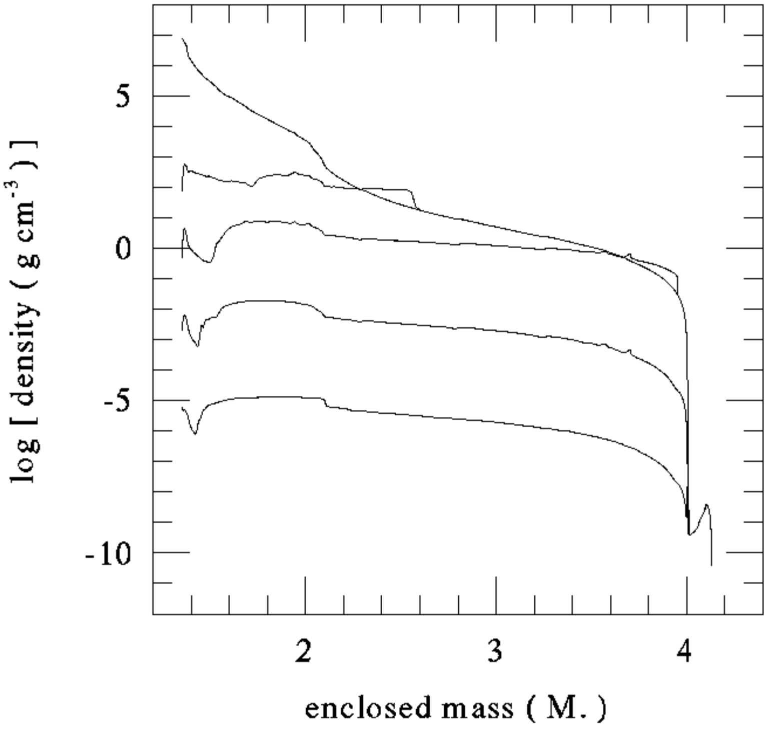
5
0
-5
-10
2
3
4
log [density (g cm^{-3})]
enclosed mass (M.)

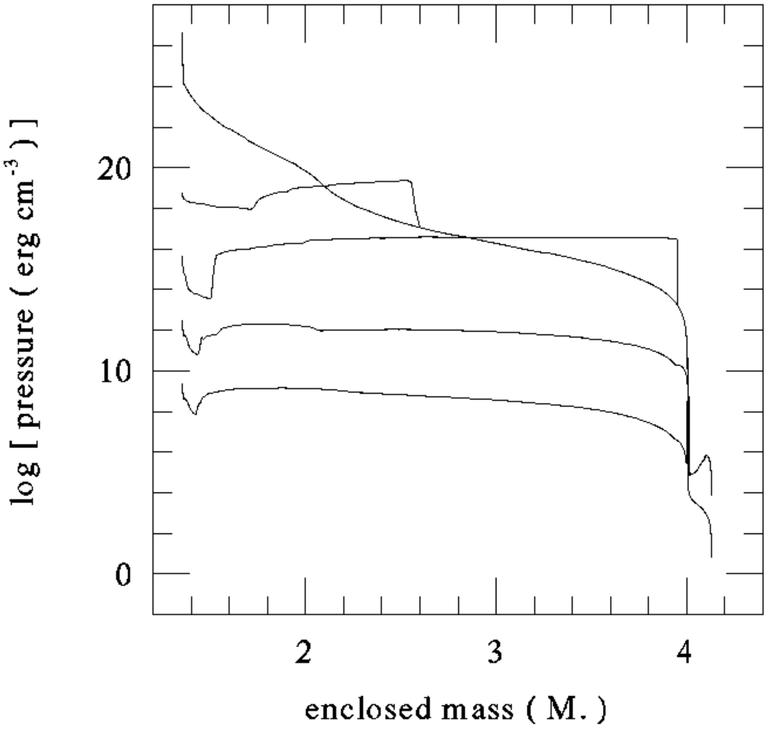
20
10
0
2
3
4
log [pressure (erg cm^{-3})]
enclosed mass (M.)

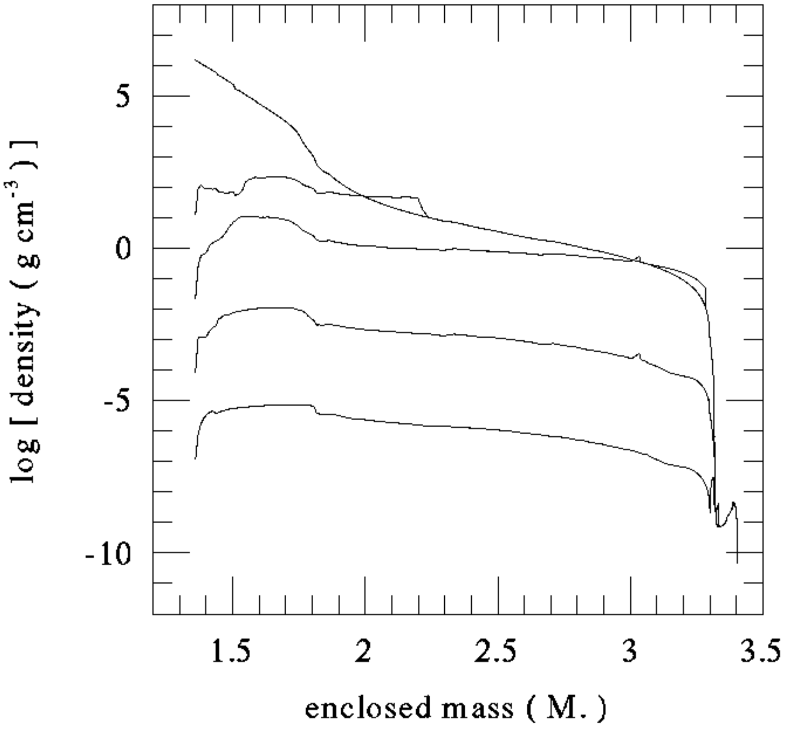
log [density (g cm^{-3})]
5
0
-5
-10
1.5
2
2.5
3
3.5
enclosed mass (M.)

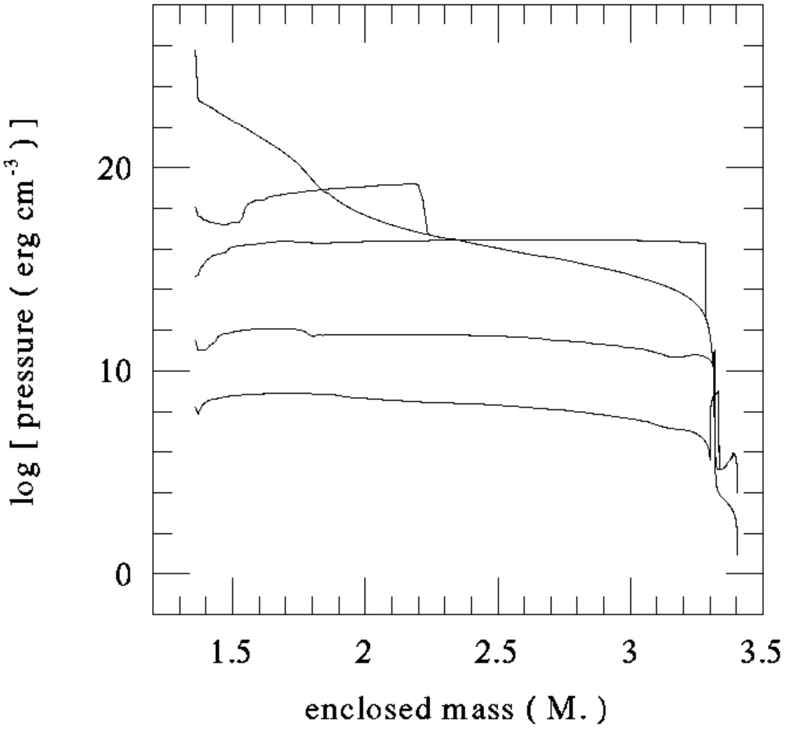
log [pressure (erg cm^{-3})]
20
10
0
1.5
2
2.5
3
3.5
enclosed mass (M.)

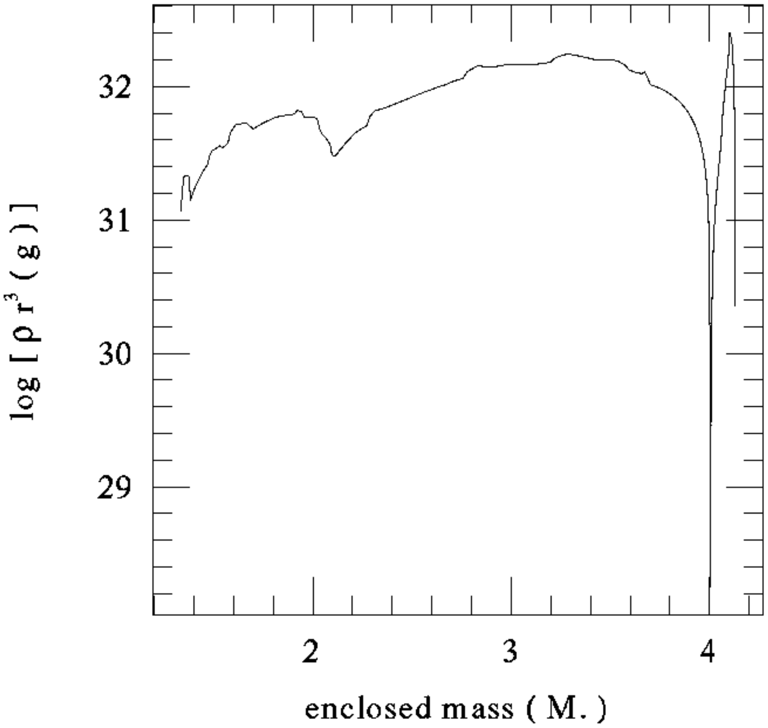

log [ρ r³ (g)]
32
31
30
29
2
3
4
enclosed mass (M.)

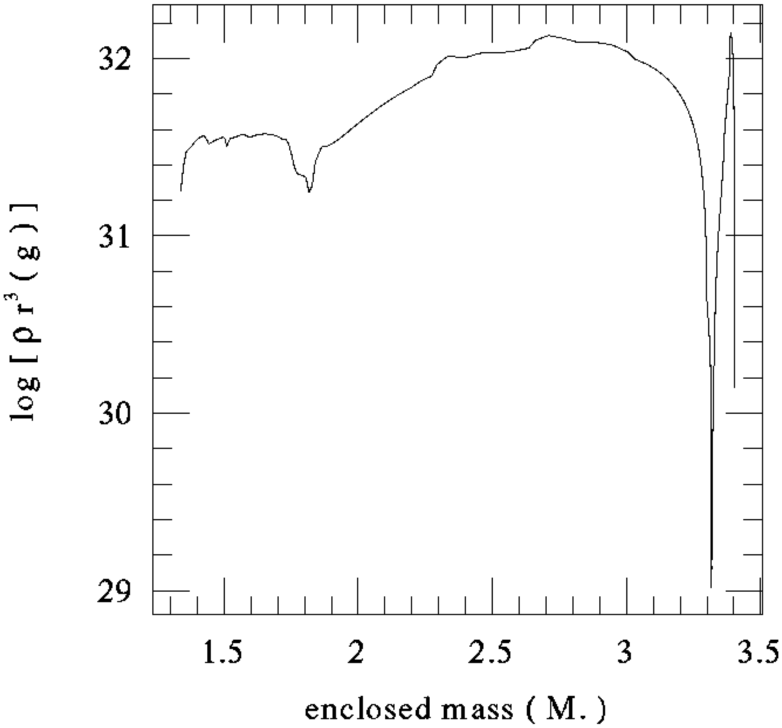

log [ρ r³ (g)]
32
31
30
29
1.5
2
2.5
3
3.5
enclosed mass (M.)

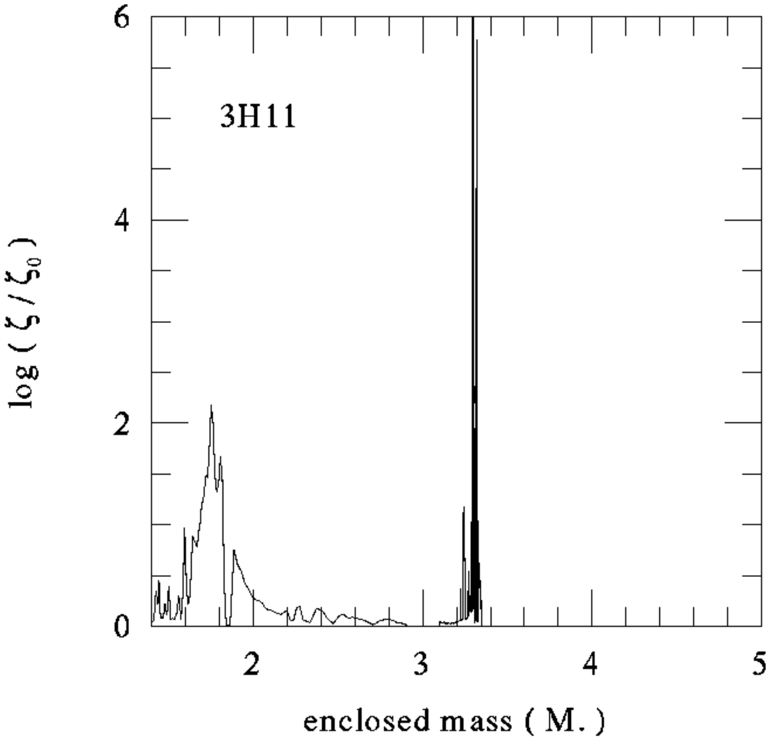
3H11
log (ζ / ζ0)
0
2
4
6
2
3
4
5
enclosed mass (M.)

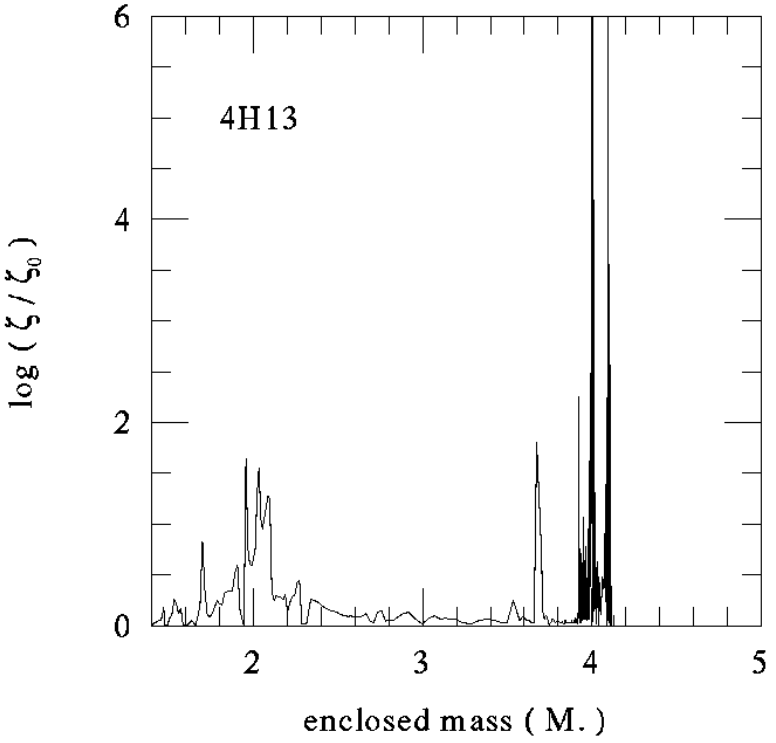
4H13
log (ζ / ζ0)
0
2
4
6
2
3
4
5
enclosed mass (M.)

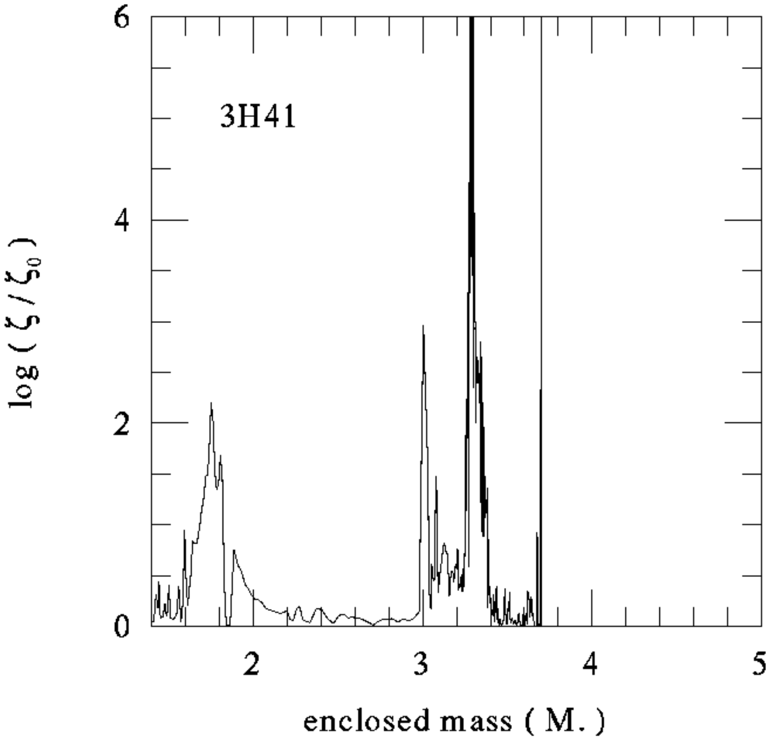
3H41
log (ζ / ζ0)
0
2
4
6
2
3
4
5
enclosed mass (M.)

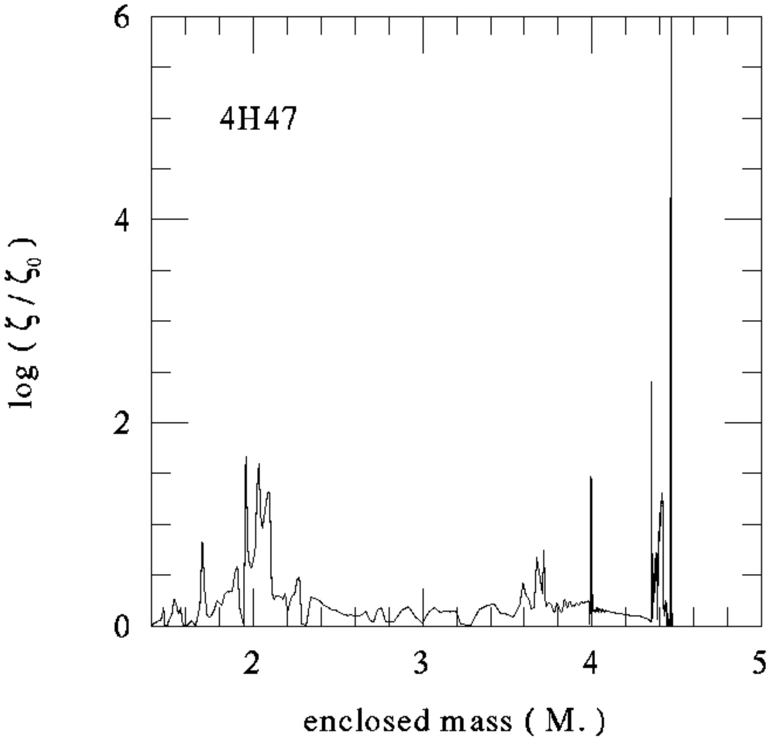
4H47
log (ζ / ζ0)
0
2
4
6
2
3
4
5
enclosed mass (M.)

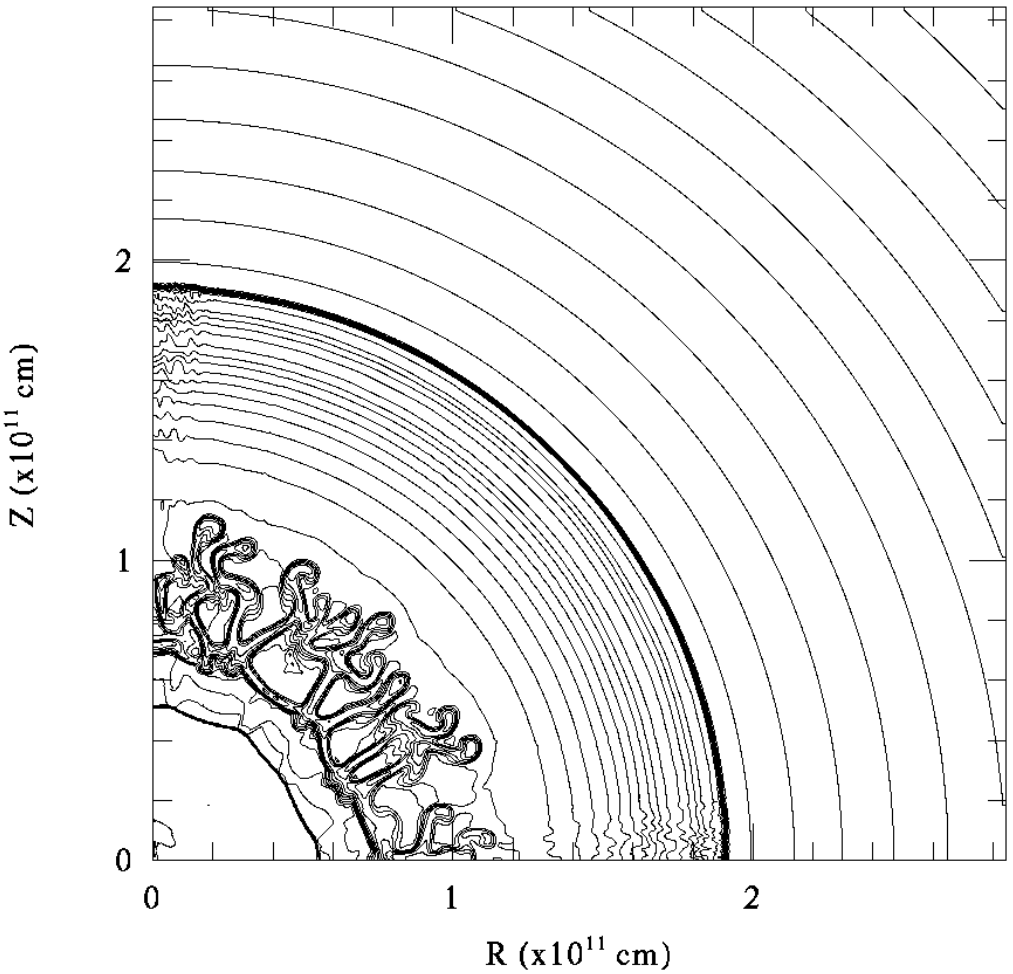
2
1
0
Z (x10^{11} cm)
0
1
2
R (x10^{11} cm)

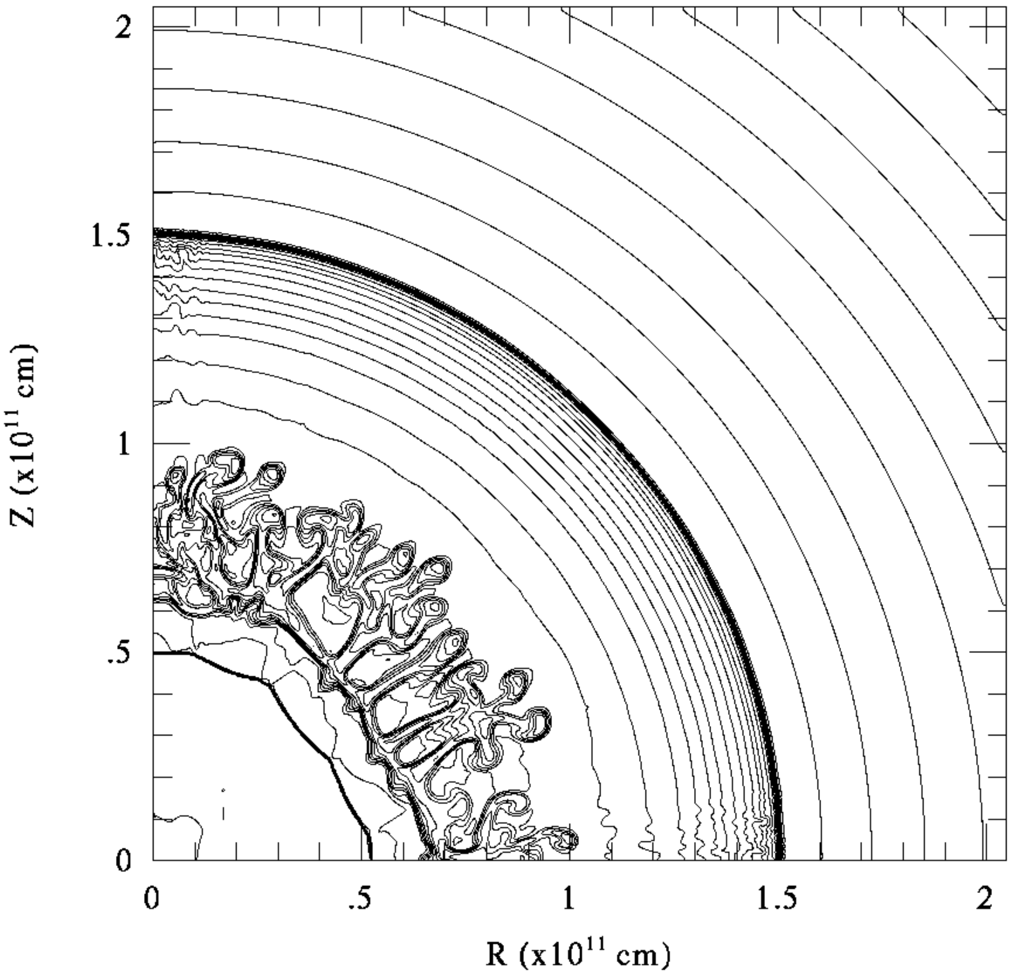

Z (x10^{11} cm)
R (x10^{11} cm)
0
.5
1
1.5
2
0
.5
1
1.5
2

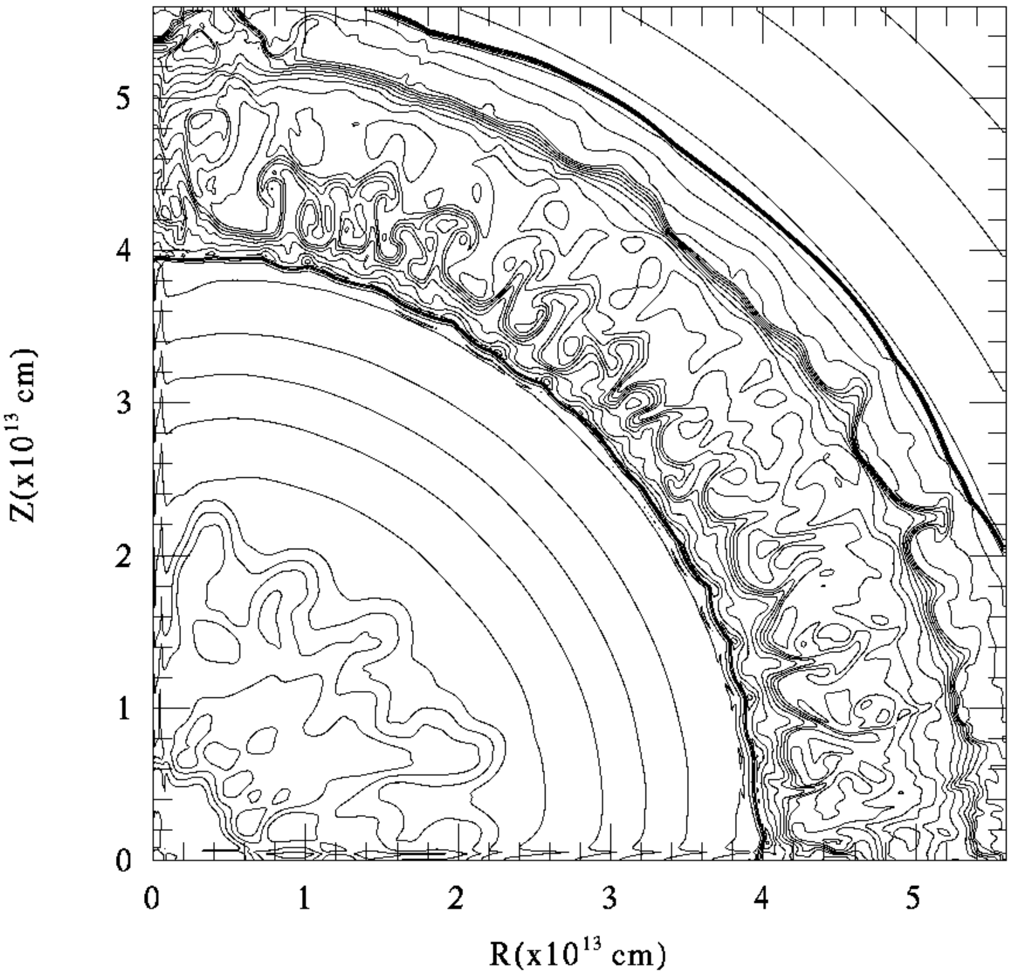
Z(x10^{13} cm)
0
1
2
3
4
5
R(x10^{13} cm)
0
1
2
3
4
5

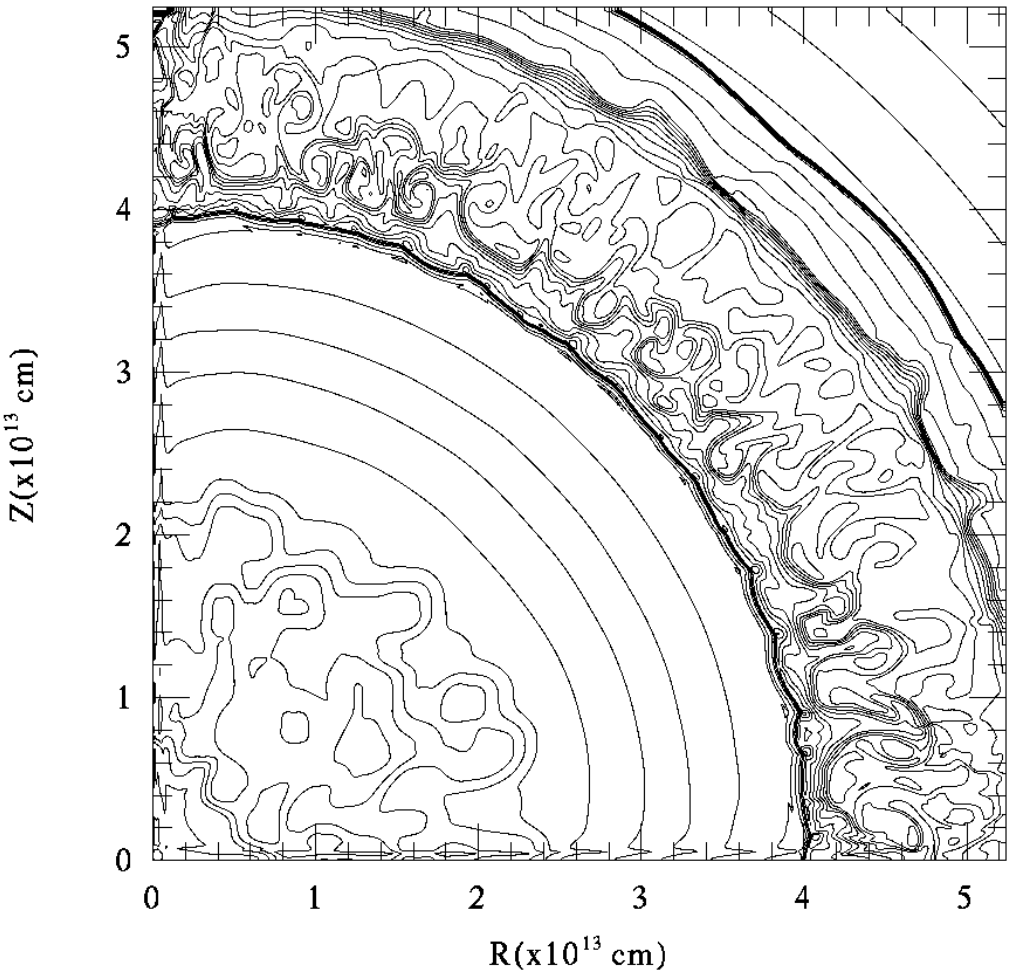
Z(x10^{13} cm)
R(x10^{13} cm)
0
1
2
3
4
5
0
1
2
3
4
5

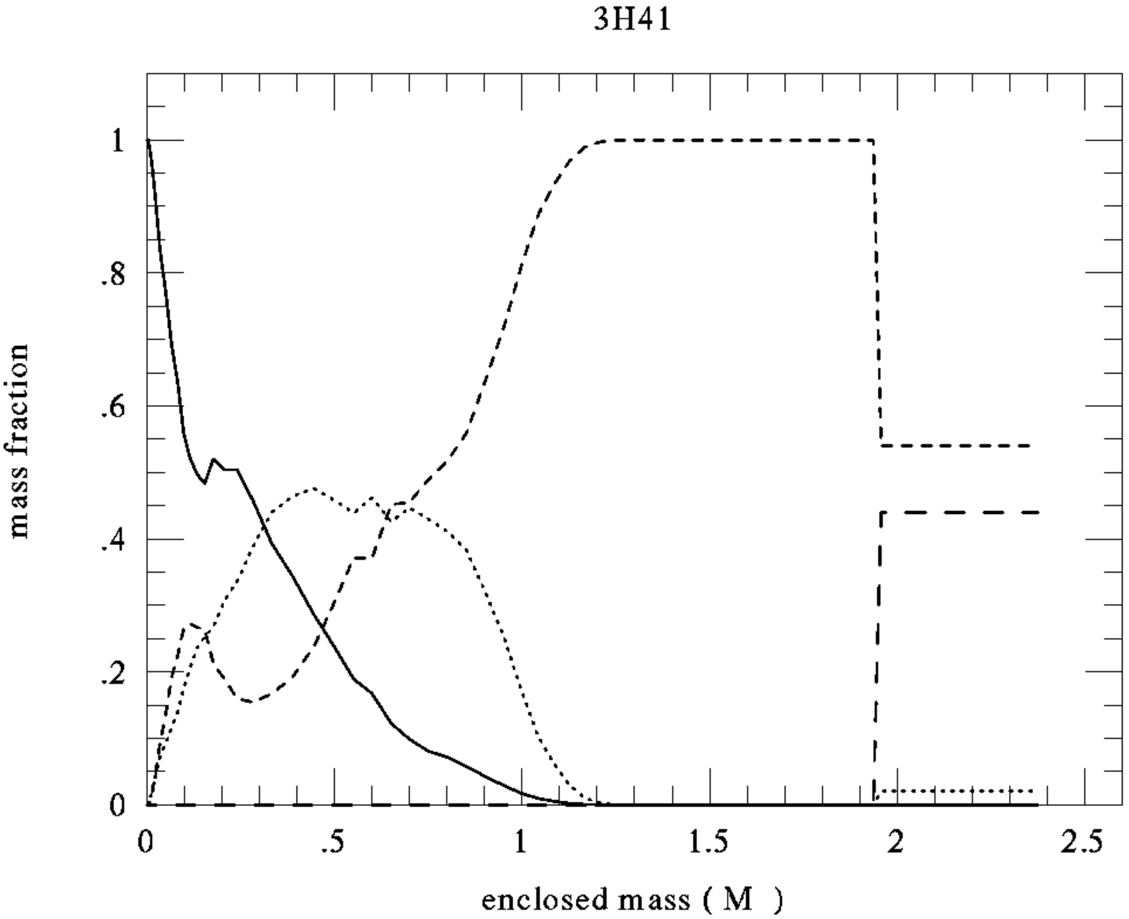
3H41
mass fraction
1
.8
.6
.4
.2
0
0
.5
1
1.5
2
2.5
enclosed mass (M)

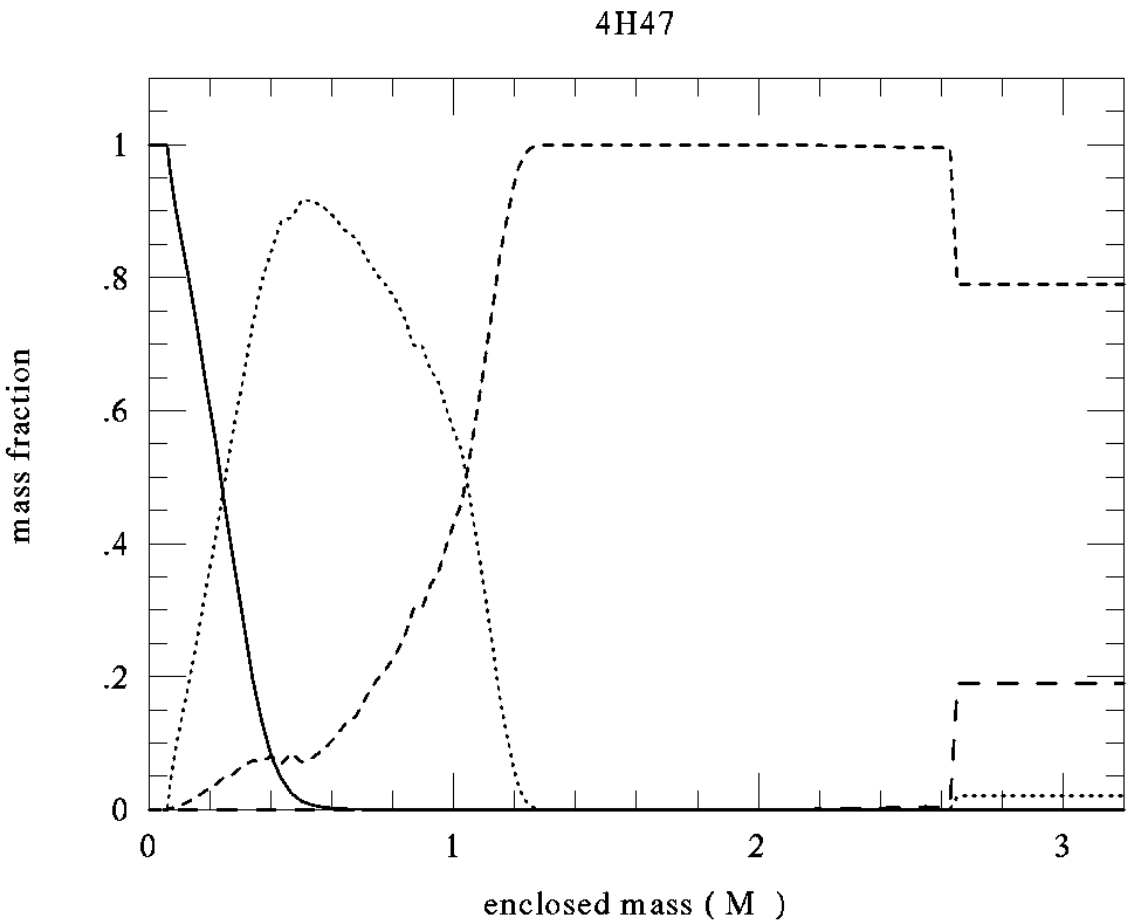
4H47
mass fraction
1
.8
.6
.4
.2
0
0
1
2
3
enclosed mass (M)

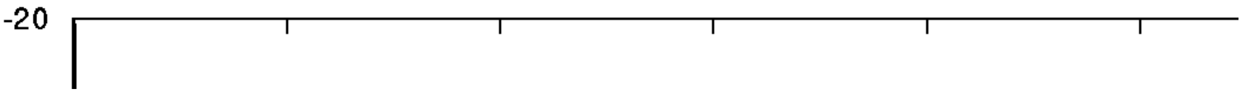
Model 3H11 and SN 1993J

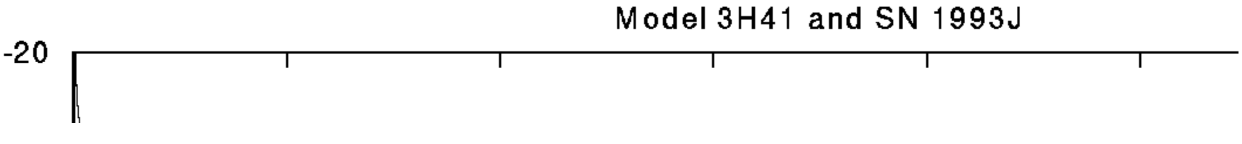
Model 3H41 and SN 1993J
-20

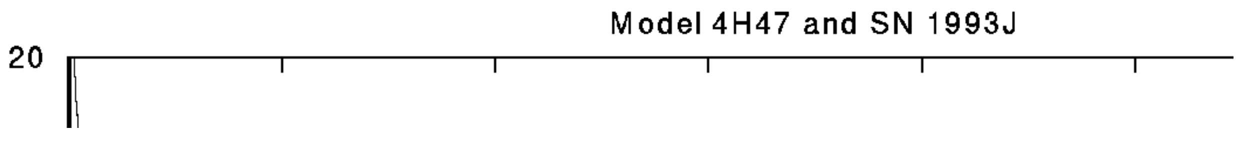
Model 4H47 and SN 1993J
20

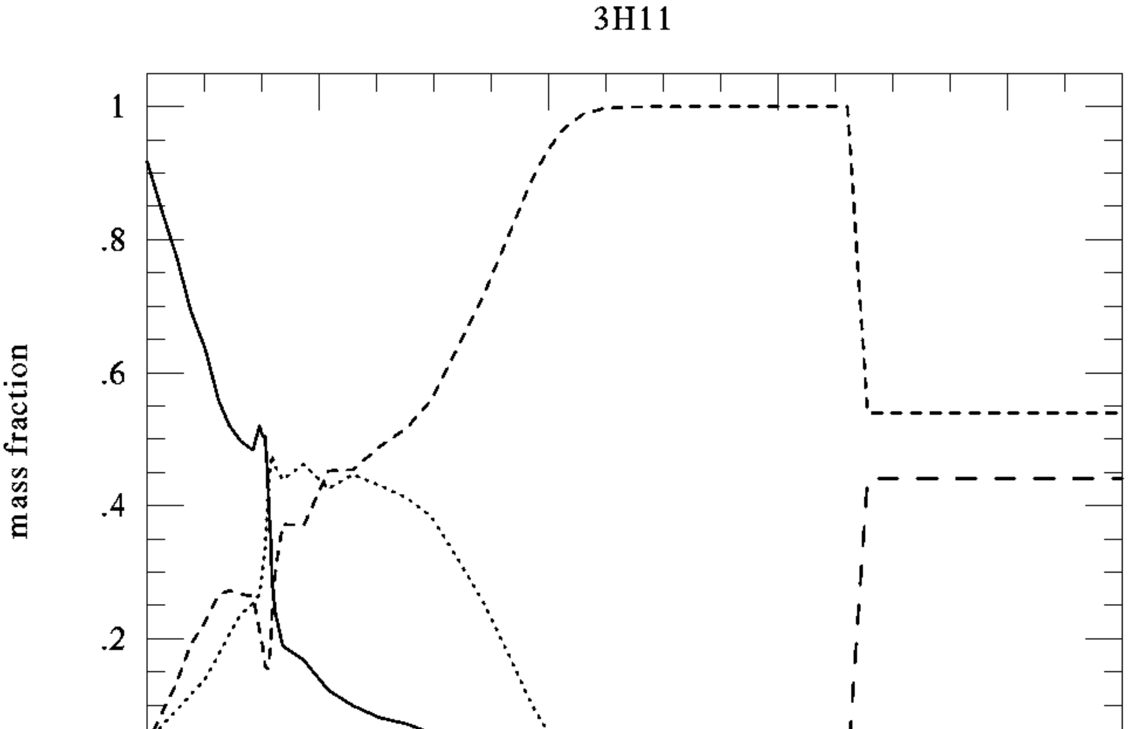
3H11
mass fraction
1
.8
.6
.4
.2
0
4000
6000
8000
10000
expansion velocity (km sec^{-1})

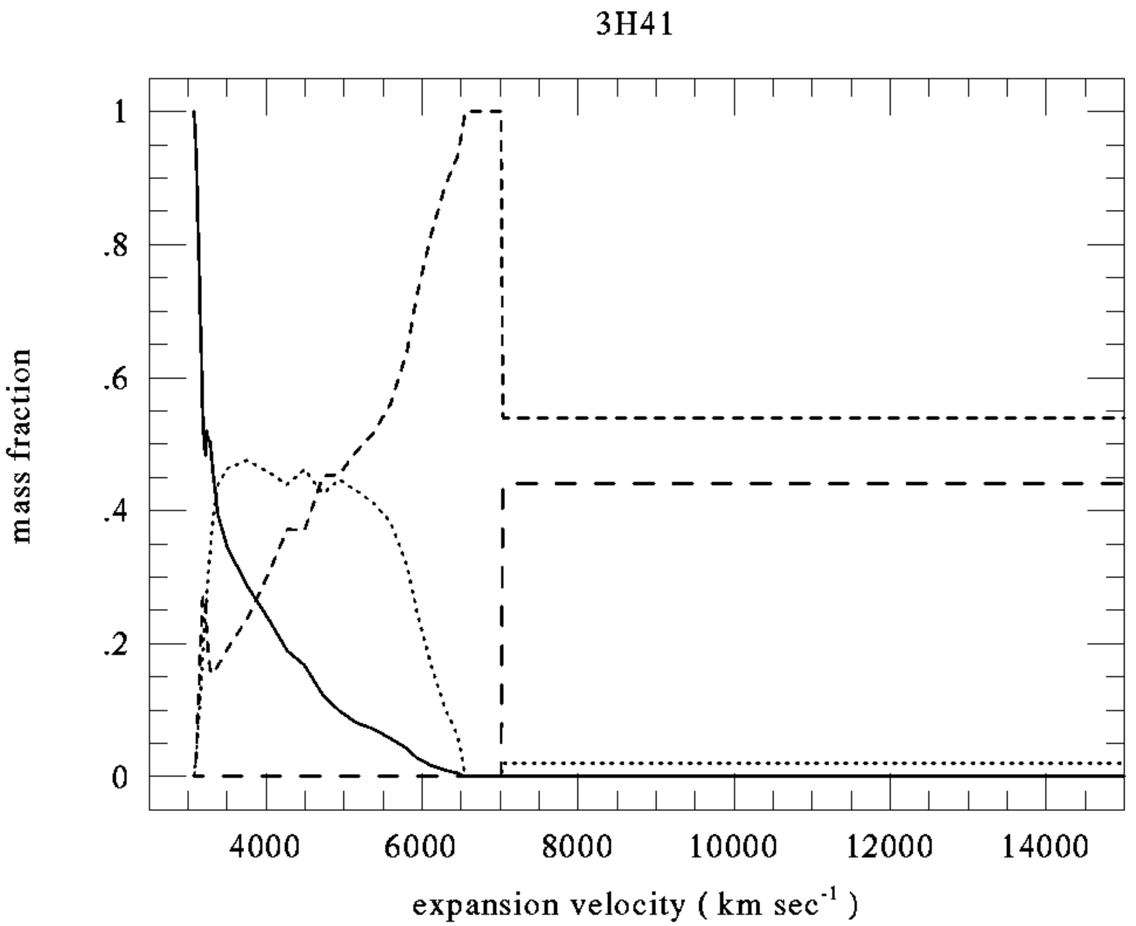
3H41
mass fraction
0
.2
.4
.6
.8
1
4000
6000
8000
10000
12000
14000
expansion velocity (km sec^{-1})

4H13

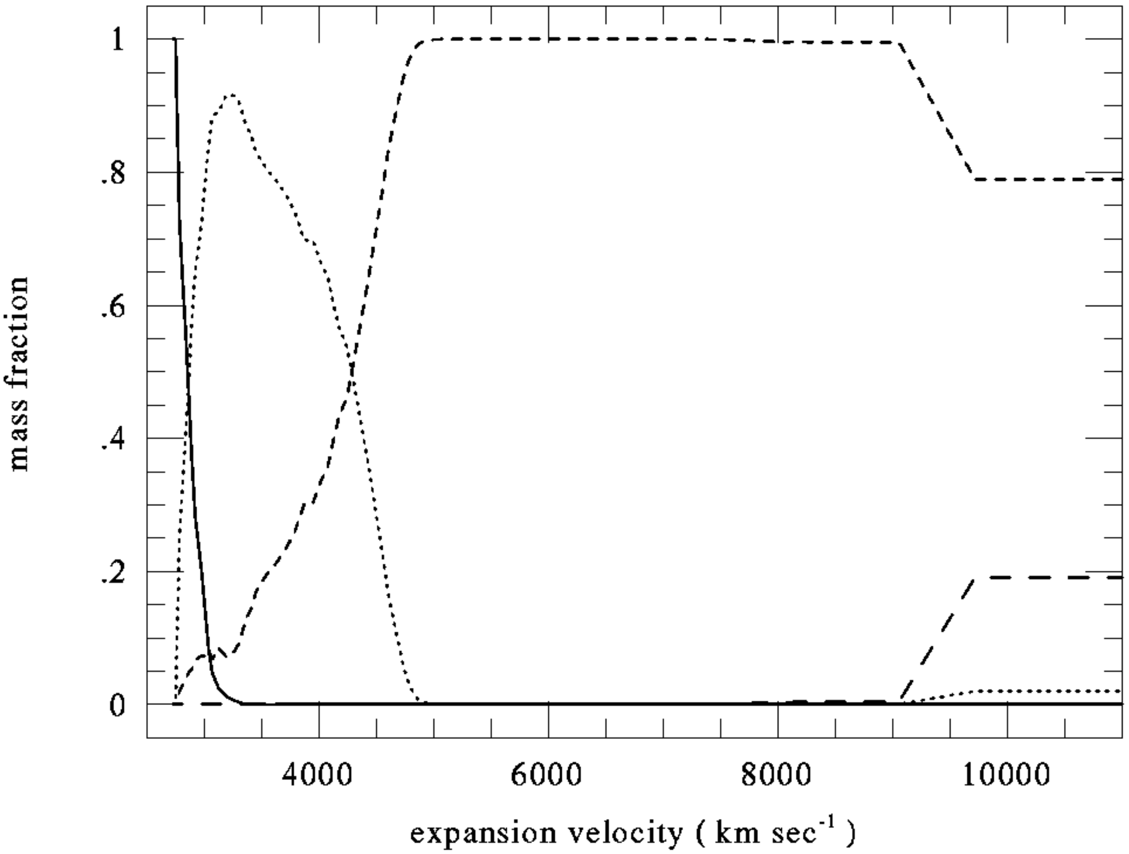

mass fraction
1
.8
.6
.4
.2
0
4000
6000
8000
10000
expansion velocity (km sec-1)

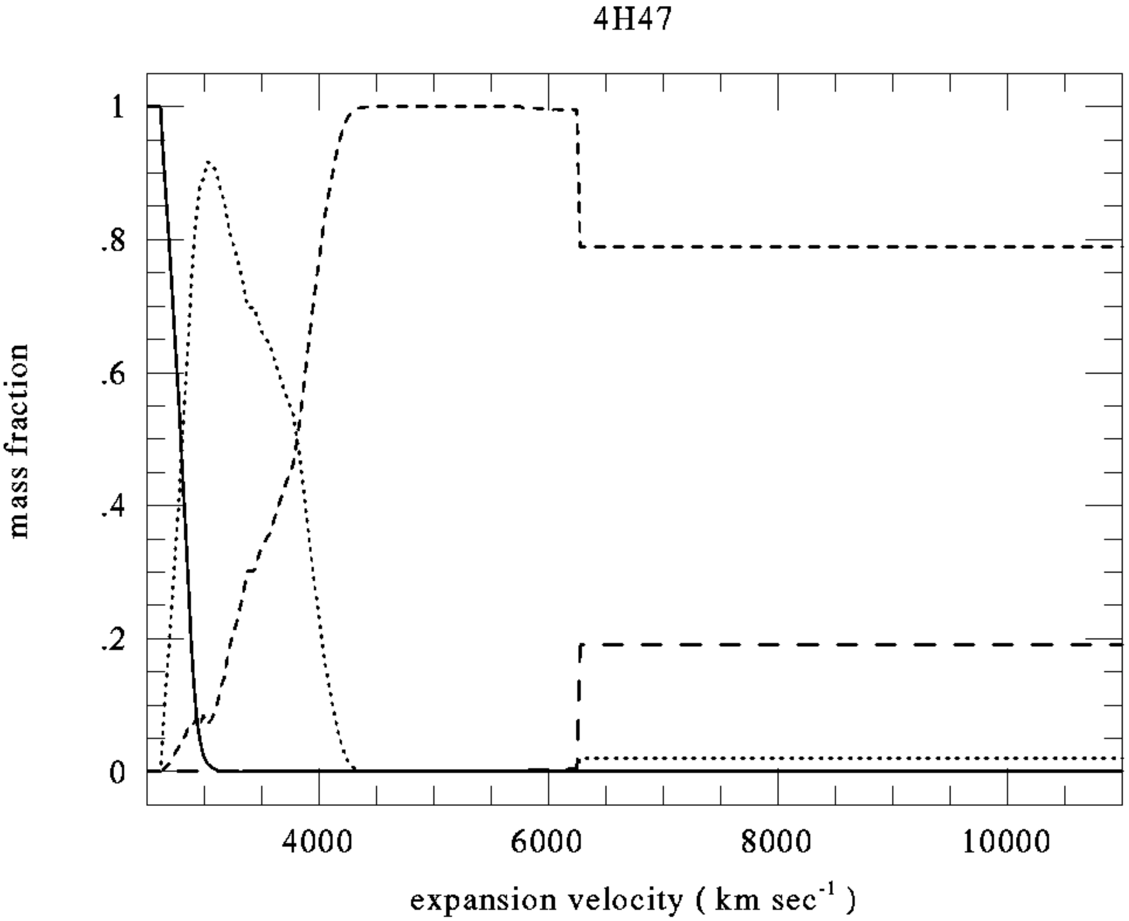
4H47
mass fraction
1
.8
.6
.4
.2
0
4000
6000
8000
10000
expansion velocity (km sec^{-1})